# Use of the GOES-R Split-Window Difference to Diagnose Deepening Low-Level Water Vapor

DANIEL T. LINDSEY

*NOAA Center for Satellite Applications and Research, Fort Collins, Colorado*

LOUIE GRASSO AND JOHN F. DOSTALEK

*Cooperative Institute for Research of the Atmosphere, Fort Collins, Colorado*

JOCHEN KERKMANN

*EUMETSAT, Darmstadt, Germany*

(Manuscript received 20 December 2013, in final form 18 April 2014)

ABSTRACT

The depth of boundary layer water vapor plays a critical role in convective cloud formation in the warm season, but numerical models often struggle with accurate predictions of above-surface moisture. Satellite retrievals of water vapor have been developed, but they are limited by the use of a model's first guess, instrument spectral resolution, horizontal footprint size, and vertical resolution. In 2016, Geostationary Operational Environmental Satellite-R (GOES-R), the first in a series of new-generation geostationary satellites, will be launched. Its Advanced Baseline Imager will provide unprecedented spectral, spatial, and temporal resolution. Among the bands are two centered at 10.35 and 12.3 $\mu$m. The brightness temperature difference between these bands is referred to as the split-window difference, and has been shown to provide information about atmospheric column water vapor. In this paper, the split-window difference is reexamined from the perspective of GOES-R and radiative transfer model simulations are used to better understand the factors controlling its value. It is shown that the simple split-window difference can provide useful information for forecasters about deepening low-level water vapor in a cloud-free environment.

## 1. Introduction

Low-level water vapor plays a significant role in deep convection and other meteorological phenomena (e.g., Moller 2001). Starting in the 1970s, many techniques have been developed to better characterize vertical profiles of moisture using remotely sensed data from satellites. Among the simplest and most fundamental methods involves satellite radiance observations at spectral bands near 11 and 12 $\mu$m. Both bands are considered to be in an atmospheric window, meaning that absorption by atmospheric gases is relatively small, but the longer-wavelength band is also called the ''dirty window'' because water vapor absorbs and emits 12-$\mu$m radiation more effectively than 11-$\mu$m radiation. The brightness temperature (BT) difference between these two bands highlights the differential water vapor absorption, and is often referred to as the split-window difference (SWD).

Chesters et al. (1983) developed a simple algorithm to retrieve lower-tropospheric water vapor using the Visible/Infrared Spin Scan-Radiometer Atmospheric Sounder (VAS) aboard one of the early Geostationary Operational Environmental Satellites (*GOES-5*). Their model used an assumed average temperature in the lower troposphere, along with observations from the 11- and 12-$\mu$m VAS bands. The satellite-observed SWD [BT (11 $\mu$m) – BT(12 $\mu$m)] depends on the vertical profiles of both water vapor and temperature, especially at low levels, so the assumption of a single average temperature leads to potentially large errors in the retrieval. Other similar methods using the SWD to retrieve atmospheric water vapor information have also been developed (e.g., Kleespies and McMillin 1990; Schroedter-Homscheidt

*Corresponding author address:* Daniel T. Lindsey, CIRA/Colorado State University, 1375 Campus Delivery, Fort Collins, CO 80523-1375.
E-mail: dan.lindsey@noaa.gov

DOI: 10.1175/JAMC-D-14-0010.1

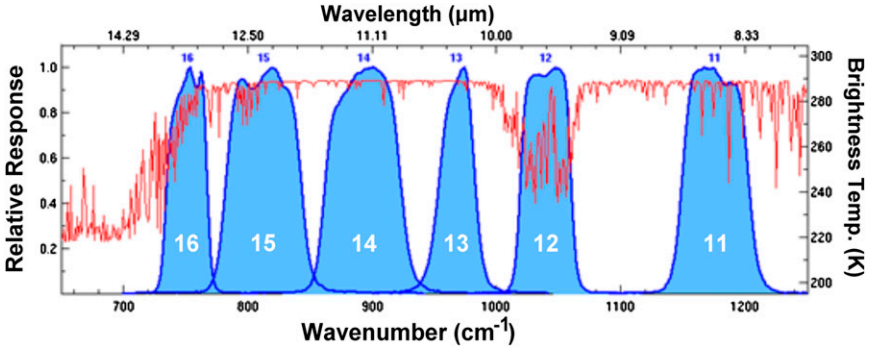


FIG. 1. Spectral response functions for ABI bands 11–16 (blue curves with band numbers indicated in white) along with the calculated absorption lines (red) from the Pressure-Layered Fast Algorithm for Atmospheric Transmittance (PFAAST) model. [Adapted from Fig. 1 of Lindsey et al. (2012).]

et al. 2008). If high-spectral-resolution observations are available from satellite, this information can be used to better constrain the retrieval (e.g., Sieglaff et al. 2009). However, the weighting functions of even narrow spectral bands are typically broad in the vertical relative to moisture profiles observed from radiosondes. Even a hyperspectral retrieval will lack the vertical resolution necessary to resolve the finescale vertical structure in the moisture profile.

The GOES sounders (Menzel and Purdom 1994) aboard *GOES-8–GOES-15* provide hourly observations with a 10-km footprint and 18 infrared (IR) spectral bands. Physical retrievals based on sounder data have been developed and implemented to run in real time (e.g., Ma et al. 1999; Li et al. 2008). These retrievals require a first guess for the temperature and moisture profiles, typically taken from the Global Forecast System (GFS) model, and validation studies have shown that the retrieved total precipitable water (TPW) provides a slight improvement to the first-guess TPW from the GFS, as verified with both radiosondes (Dostalek and Schmit 2001) and surface-based microwave-measured TPW (Li et al. 2008).

In 2016, the first in a new generation of operational geostationary satellites (GOES-R) will be launched. Its primary instrument is the Advanced Baseline Imager (ABI; Schmit et al. 2005), which will provide regular 5-min imagery with a footprint of 2 km at nadir for 11 spectral bands between 2.25 and 13.3 $\mu$m. GOES-R will not carry an atmospheric sounder, so the ABI will be used to collect temperature and moisture retrievals similar to those from the current GOES sounder, referred to as "legacy retrievals" (e.g., Jin et al. 2008; Lee et al. 2014). Schmit et al. (2008) showed that the ABI's legacy retrievals will provide an adequate substitution to the sounder retrievals, but are not quite as accurate due to coarse vertical resolution. In addition, the legacy retrievals will have 10-km horizontal resolution, despite the availability of 2-km IR data from the ABI.

Among the IR bands planned for the ABI are two window bands (10.35 and 11.2 $\mu$m; bands 13 and 14 in Fig. 1, respectively) and one band in the dirty window (12.3 $\mu$m; band 15 in Fig. 1). Lindsey et al. (2012) showed that the 10.35-$\mu$m band is cleaner with respect to water vapor absorption than is the 11.2-$\mu$m band, so it will be used as the clean window to form the ABI SWD [BT (10.35 $\mu$m) – BT(12.3 $\mu$m)] in the forthcoming simulations. Previous GOES imagers (*GOES-8–GOES-11*) had a dirty window band, but their SWDs (10.7–12.0 $\mu$m) were noisy and striped because of relatively poor signal-to-noise ratios relative to what is planned for the ABI. The new imager's specifications include improved radiometrics (Schmit et al. 2005) that should significantly reduce the striping and allow for less-noisy SWD imagery at better resolution.

Given the limitations and uncertainties outlined above with quantitative water vapor retrievals using the ABI, we seek to investigate whether the SWD alone will provide useful information about low-level water vapor. The formation and evolution of convection depends strongly on the detailed structure of the low-level moisture field. Increases in low-level (say, from surface to 700 hPa) column water vapor often signal low-level mass convergence, which is typically associated with rising motion and sometimes convective initiation. Therefore, any satellite product that can provide useful information about boundary layer water vapor with a 2–3-km footprint and its temporal change on time scales of 5 min will potentially be a great help to operational forecasters. Section 2 provides idealized radiative transfer model (RTM) simulations, section 3 presents some more realistic simulations based on cloud model output, and section 4 offers some examples of real data from Meteosat Second Generation (MSG). Section 5 will summarize the findings.

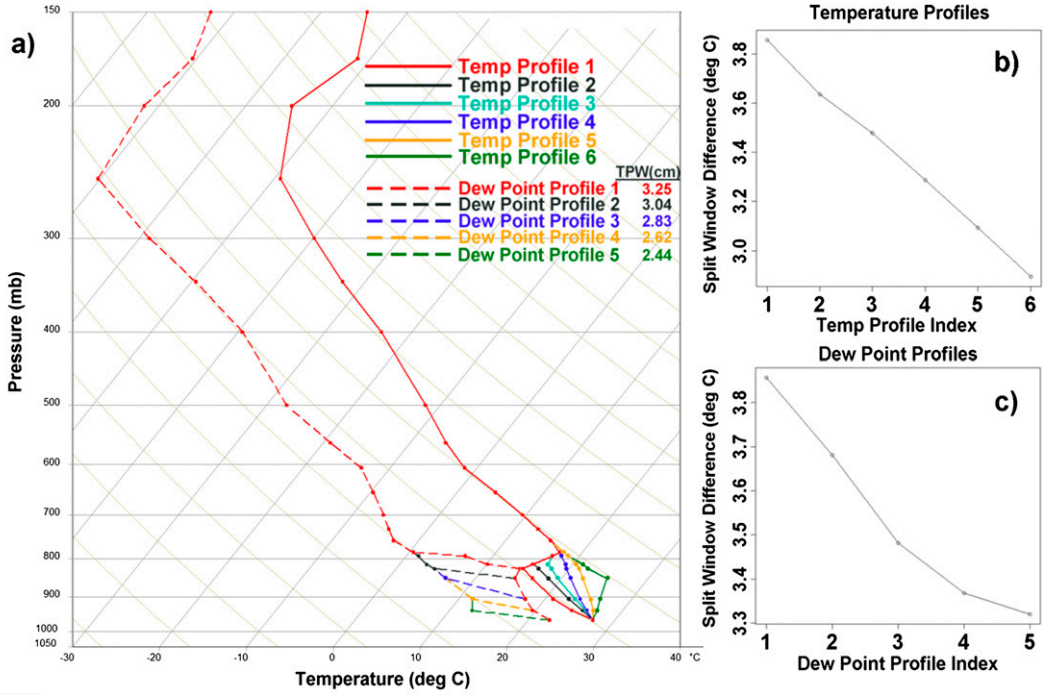


FIG. 2. (a) Six different temperature profiles and five different dewpoint profiles used in the sensitivity experiments described in the text shown on a skew $T$–log$p$ diagram. TPW (cm) is listed next to each of the dewpoint profiles. (b) CRTM-generated split-window difference value using dewpoint profile 1 with the six different temperature profiles. (c) As in (b), but for temperature profile 1 along with the five different dewpoint profiles.

## 2. Idealized RTM simulations

To test the sensitivity of satellite-observed SWDs to changes in lower-tropospheric temperature and water vapor profiles, the Community Radiative Transfer Model (CRTM; Han et al. 2006) was used to estimate the ABI-detected brightness temperatures of bands 13 and 14. The CRTM takes into account the details of each bands' spectral response function. Sounding data from Norman, Oklahoma, at 1800 UTC 20 May 2013 (the red lines in Fig. 2a) were used as the initial input to the CRTM. The satellite is assumed to be in the position of the current GOES-East (at a longitude of 75°W), and these simulations are done over the central U.S. plains, resulting in realistic satellite zenith angles. Temperature sensitivity tests were performed by holding the dewpoint profile constant (dewpoint profile 1) and altering the temperature profile at levels from just above the surface to near 780 mb (Fig. 2a) in a cloud-free atmosphere. Temperature profile 1 (from the observed Norman sounding) was nearly dry adiabatic from the surface to 820 mb (Fig. 2a) with relatively large amounts of water vapor in the boundary layer. Above, a sharp inversion served to keep the relatively drier air aloft from easily mixing downward. This sounding results in an SWD value of +3.9°C (Fig. 2b), meaning the simulated 10.35-$\mu$m brightness temperature is 3.9°C warmer than the 12.3-$\mu$m brightness temperature. Cooler values at 12.3 $\mu$m are primarily due to water vapor within the boundary layer absorbing and reemitting 12.3-$\mu$m radiation at a colder temperature, due to the temperature's decrease with height.

Temperature profiles 2–6 have the same surface temperature as the initial simulation, but the temperature decreases with height less sharply with each profile (Fig. 2a). The result is a warmer boundary layer, where most of the water vapor exists. Figure 2b shows that the more stable and warmer profiles result in lower SWD values because differential water vapor absorption at 12.3 $\mu$m compared to 10.35 $\mu$m becomes less of a factor as the boundary layer temperature approaches the surface temperature. Therefore, the atmospheric profiles with steeper low-level lapse rates will produce larger positive SWD values.

For the moisture sensitivity tests, temperature profile 1 was used and held constant while the boundary layer moisture depth was decreased (dashed lines in Fig. 2a). The TPW values for each dewpoint profile are shown in Fig. 2a, and decrease from 3.25 to 2.44 cm. Figure 2c shows the CRTM SWD values. As the depth of the low-level moisture (and the corresponding total water in the column) decreases, the SWD also decreases. These results suggest that for a given temperature profile, observed

TABLE 1. CRTM BTs for various surface emissivity values.

| $EMIS_{10.35}$ | $EMIS_{12.3}$ | 10.35-$\mu$m BT (°C) | 12.3-$\mu$m BT (°C) | SWD (°C) |
|---|---|---|---|---|
| 1.0 | 1.0 | 22.1572 | 18.2999 | 3.8573 |
| 0.96523 | 0.97379 | 21.4252 | 18.0794 | 3.3458 |
| 0.97163 | 0.97313 | 21.5552 | 18.0738 | 3.4814 |

changes in the satellite-measured SWD can provide information about the depth of the low-level moisture.

Another factor that affects satellite-observed brightness temperatures in clear skies is surface emissivity, which varies both spatially and spectrally. In the CRTM simulations presented in Fig. 2, surface emissivity values of 1.0 were used for both 10.35 and 12.3 $\mu$m. To test the sensitivity of SWD to more realistic emissivity values, a dataset containing monthly mean, spectrally dependent surface emissivity values (Seemann et al. 2008) was obtained. Using the map from May, surface emissivity values in Texas were examined and two points 125 km apart were chosen that had a relative maximum in the difference between the emissivity at 10.35 and 12.3 $\mu$m. Table 1 shows these values, along with the resulting 10.35- and 12.3-$\mu$m BTs (and the resulting SWD) simulated from the CRTM. The base-case sounding above was used in all three simulations. With more realistic surface emissivity values, compared with assuming that both were 1.0 as in the base case, values of the SWD decreased by approximately 0.5°C. But more importantly, the difference in SWD between the two points in Texas (rows 2 and 3 in Table 1) is ~0.13°C, similar to the SWD change between dewpoint profiles 3 and 4 shown in Fig. 2c. This test shows that satellite-observed spatial variations in SWD of up to ~0.15°C can be explained by surface emissivity heterogeneity. It should be noted that the values chosen from Texas are comparable to the maximum horizontal variations in other portions of the central U.S. plains. In practice, viewing a time animation of the SWD, as will be possible with GOES-R, will help identify local maxima in the SWD associated with surface emissivity because they will remain stationary with time.

## 3. Simulated imagery from the NSSL WRF

### *a. SWD from 20 May 2013*

More realistic simulations are possible by taking output from a high-resolution numerical model and using that as input into a radiative transfer model in order to get a field of brightness temperatures over a large domain. This method has been routinely performed for several years (Bikos et al. 2012) using output from the 0000 UTC run of the 4-km National Severe Storms Laboratory's (NSSL) Advanced Research core in the Weather Research and Forecasting (WRF) Model (ARW; Kain et al. 2010). Three-dimensional fields of temperature, water vapor, model level heights, cloud water, cloud ice, snow, graupel, and rain, along with the two-dimensional field of canopy temperature, are fed into the Cooperative Institute for Research in the Atmosphere (CIRA) RTM [see Bikos et al. (2012) for model details], which then outputs simulated brightness temperatures at various GOES-R ABI bands, including the 10.35- and 12.3-$\mu$m bands. A geostationary satellite position at 75°W is assumed. The Seemann et al. (2008) monthly mean surface emissivity dataset is used in the model simulations. Forecast imagery is available every hour out to 36 h. A major advantage of using simulated imagery from high-resolution model output is the ability to look at the model fields themselves to know the exact state of the atmosphere resulting in the simulated brightness temperature fields.

Multiple good examples of the utility of SWD in diagnosing low-level water vapor increases have been collected since simulated imagery generation from the NSSL WRF began in 2011, but here we will highlight a recent case from 20 May 2013. This day made headlines due to a significant tornado that affected Moore, Oklahoma. The 0000 UTC run of the NSSL WRF on 20 May 2013 did a reasonably good job of simulating the synoptic conditions, but a comparison between the model and observations is not shown. The purpose here is instead to assume that the model is reality and to examine the relationship between the model conditions and the associated simulated satellite data. A surface dryline extended southwestward from an area of surface low pressure in central Oklahoma (Fig. 3). Surface convergence along the dewpoint gradient in Texas can be inferred from the surface wind vectors in Fig. 3. The simulated 10.35-$\mu$m IR window band and the simulated SWD are shown for the forecasts valid from 1800 to 2100 UTC in Fig. 4. Low clouds in central Oklahoma (Fig. 4a) prevent any useful information from the SWD field there, but clear skies near the dryline in Texas provide ideal conditions for examining low-level moisture. Cloud cover results in an SWD field that is muddied and unusable, so this technique requires clear skies. At 1800 UTC, a local maximum in SWD exists across central Texas in the vicinity of the dryline (Fig. 4b), with maximum values near +7°C. As the afternoon progresses, the SWD maximum remains in a similar location and its magnitude slightly increases (Figs. 4d,f,h). Convective clouds begin to form along the dryline and within the region of the SWD maximum at 1900 UTC (Fig. 4c), and convection initiates in central Texas shortly afterward (Figs. 4e,g).

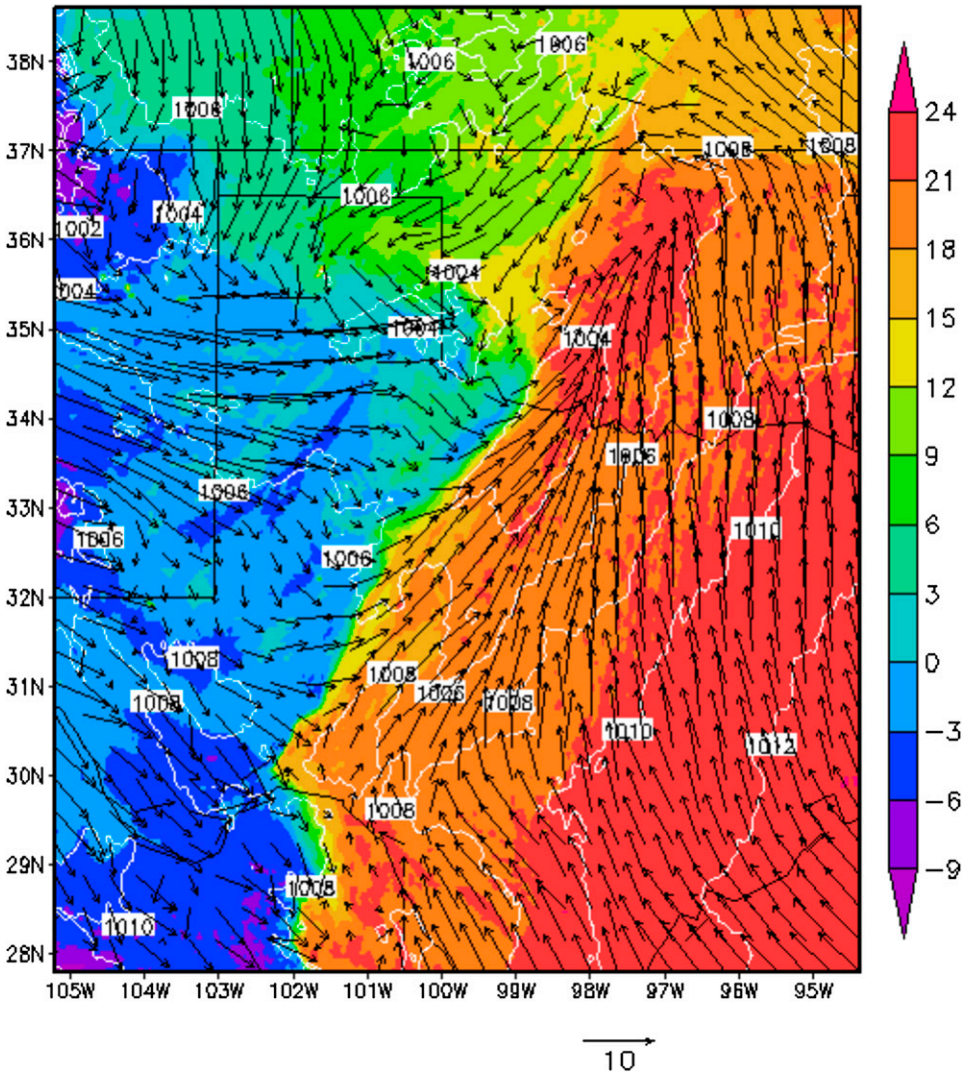


FIG. 3. NSSL WRF 17-h forecast from the 0000 UTC 20 May 2013 cycle, valid at 1700 UTC, showing surface dewpoint as colors (°C), mean sea level pressure in white contours (hPa), and surface wind vectors ($m\,s^{-1}$).

The sensitivity test results presented in Fig. 2 show that integrated low-level water vapor content and the temperature lapse rate (LR) within that layer affect the SWD. We define an approximation for the surface-to-700-hPa lapse rate as

$$\mathrm{LR} = \frac{T_{\mathrm{sfc}} - T_{700}}{\dfrac{T_{\mathrm{sfc}} + T_{700}}{2} \times \dfrac{R_d}{g} \ln\left(\dfrac{p_{\mathrm{sfc}}}{700}\right)}, \qquad (1)$$

where $T_{\mathrm{sfc}}$ and $T_{700}$ are the surface and 700-hPa temperatures (K), respectively; $p_{\mathrm{sfc}}$ is the surface pressure (hPa); $R_d$ is the gas constant for dry air; and $g$ is the acceleration due to gravity. Another way to view the dependence of SWD on the water vapor field is via a vertical cross section of the model output. Figure 5 shows the values of specific humidity in the vertical through the line shown in Fig. 4b, along with line plots of LR from Eq. (1) and the SWD. Deeper water vapor can be seen east of 100°W, with a broad maximum near the dryline between 100° and 99°W. The SWD peaks in that same region, and shows values in the 4°–5°C range in the warm sector of east Texas. Lapse rate values are unusually high, especially in west Texas, because the surface temperature is strongly affected by the very hot ground temperatures, resulting in a superadiabatic layer near the surface. Steep lapse rates in west Texas do not result in large SWD values because the water vapor content in this region is too small. The largest SWD

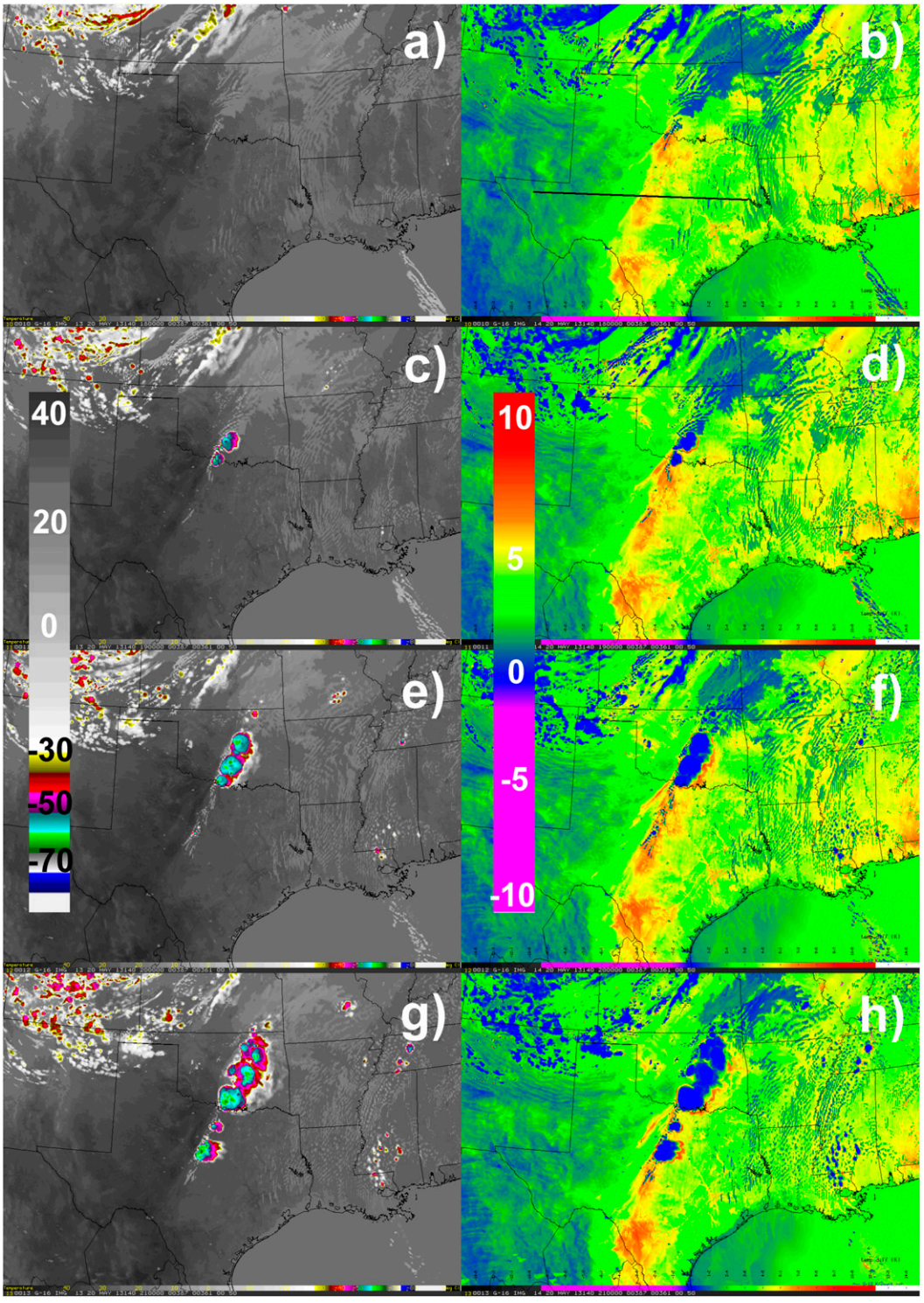


FIG. 4. (a),(c),(e),(g) Simulated 10.35-$\mu$m and (b),(d),(f),(h) SWD [BT(10.35 $\mu$m)–BT(12.3 $\mu$m)] imagery based on the (a),(b) 18-, (c),(d) 19-, (e),(f) 20-, and (g),(h) 21-h forecasts of the NSSL WRF initialized at 0000 UTC 20 May 2013, valid at 1800–2100 UTC 20 May 2013. The BT and SWD units are °C. The horizontal black line in (b) is the location of the vertical cross section shown in Fig. 5.

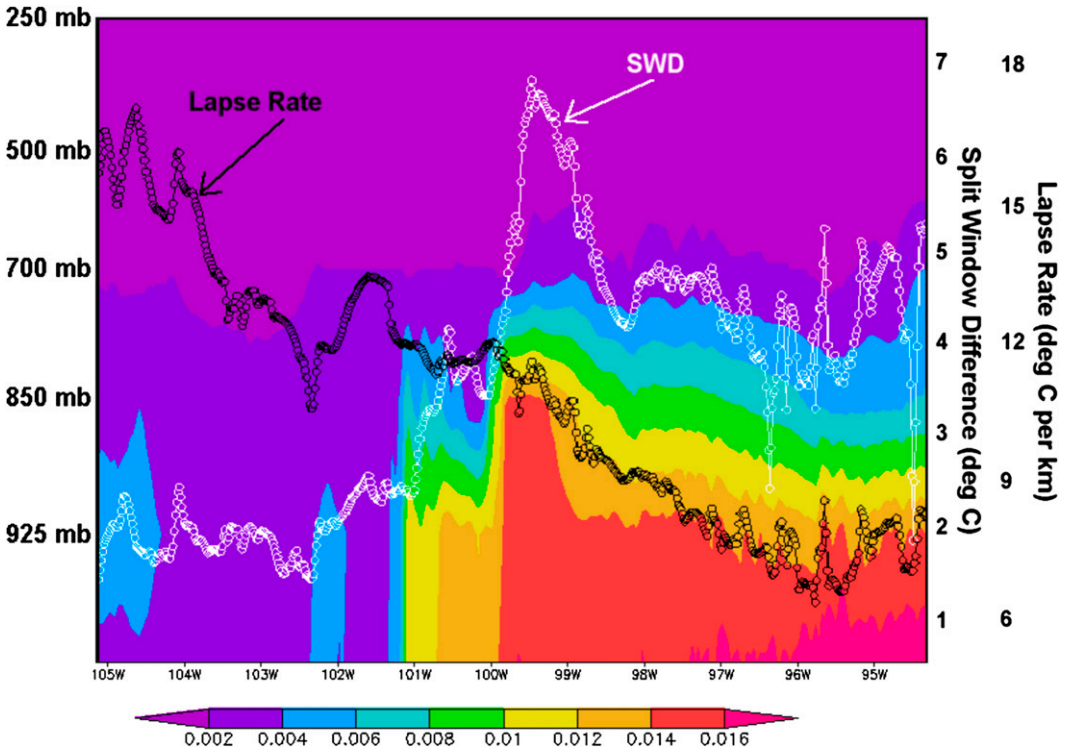


FIG. 5. West–east vertical cross section through the line in Fig. 4b showing the specific humidity (colors; kilograms of water vapor per kilogram of air), the SWD (°C), and lapse rate [from Eq. (1); °C km$^{-1}$], from the 18-h forecast of the NSSL WRF valid at 1800 UTC 20 May 2013. The specific humidity is plotted as a function of pressure on the left axis and longitude along the bottom, and the SWD and LR are functions of longitude, with their scales on the right axis.

values exist where the low-level water vapor is deepest within a region where temperatures decrease with height. Note that surface water vapor values are fairly constant east of the dryline, increasing in extreme east Texas, yet the SWD is largest near the dryline. This shows that satellite-observed SWD is providing more information about the depth of the moisture than about the magnitude of the surface water vapor content. Since numerical models (and therefore hourly analyses of 925-hPa water vapor, for example) often struggle with accurately predicting water vapor content just above the surface, qualitative use of the SWD can help forecasters identify regions of locally deeper water vapor, such as along the surface dryline in the 20 May 2013 example. Viewing an animation of SWD changing with time will allow forecasters to easily identify locally deepening water vapor in an environment of steep lapse rates.

### b. *Noise and striping analysis*

The simulated results presented above are based purely on model output and therefore do not include satellite instrument noise that may occur. Specifications for the ABI require that the noise equivalent change in temperature (NEdT) for the 10.35- and 12.3-$\mu$m bands be less than 0.1°C for a scene at 27°C, but the actual worst-case estimate from the ABI vendor is 0.05°C (Griffith et al. 2011). To introduce the effect of noise into the SWD analysis, we used the simulated data from 1800 UTC 20 May 2013 and added a random number between −0.1° and +0.1°C to all simulated brightness temperatures at both bands. The resulting SWD image is shown in Fig. 6a. In comparison with Fig. 4b, the differences are difficult to detect. This is because the maximum difference in SWD between Figs. 4b and 6a is 0.2°C, and the color table has only minimal differences in color for a range so small. Values of ±0.1°C were used even though the vendor-estimated worst case is ±0.05°C, so instrument noise will likely have a negligible impact on the SWD.

A similar analysis can be performed to simulate striping. Image striping occurs because different sensors scan successive lines; the ABI has 16 sensors scanning simultaneously, so every 16th line will be scanned by the same sensor. Each sensor may have a slight bias relative to the others. The magnitude of the bias due to striping, as with the noise analysis, is assumed to be 0.1°C. A bias of +0.1°C was added to horizontal lines 1, 3, 5, . . . , (i.e., all odd-numbered rows in the model from the northern

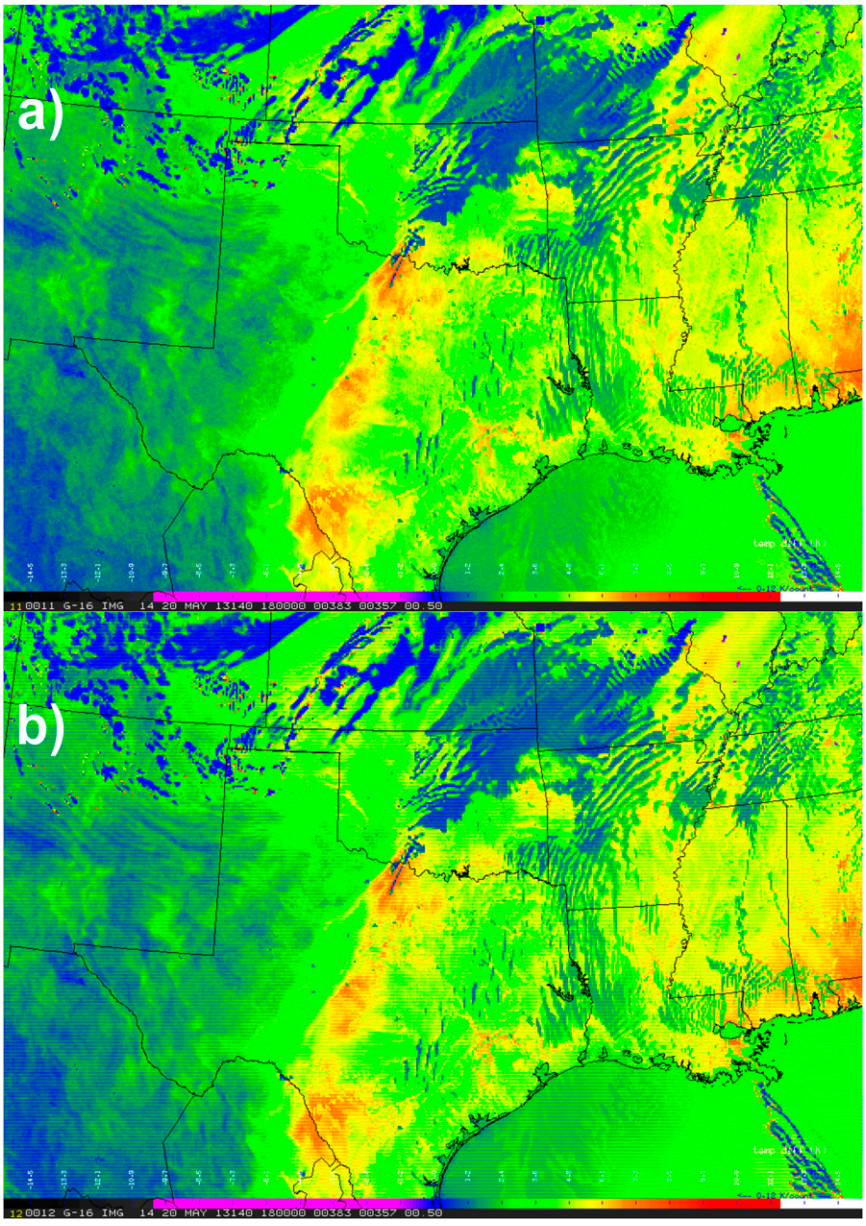


FIG. 6. As in Fig. 4b, but (a) with a random value between −0.1 and +0.1 K added to each simulated BT before computing the SWD to simulate a worst-case scenario for instrument noise and (b) with +0.1 K added to every second horizontal line and −0.1 K added to the remaining lines for the 10.35-$\mu$m simulated BTs, and −0.1 K added to every second horizontal line and +0.1 K added to the remaining lines for the 12.3-$\mu$m simulated BTs, before the SWD is computed. The result is a worst-case estimate for ABI striping.

to the southern boundary), and a bias of −0.1°C was added to lines 2, 4, 6, . . . , for the 10.35-$\mu$m simulated brightness temperatures. Next, the same was applied to the simulated 12.3-$\mu$m brightness temperatures, except that −0.1°C was used for lines 1, 3, 5, . . . , and +0.1 K for lines 2, 4, 6, . . . . The modified image (Fig. 6b) thus has 10.35–12.3-$\mu$m SWD values for the odd-numbered lines that are 0.2°C larger than in the original case (Fig. 4b) and SWD values for the even-numbered lines that are 0.2°C smaller than in the original case. In looking closely at Fig. 6b, the imposed striping can be seen as the subtle discontinuity in SWD from one horizontal line to the next. The magnitude of the striping is considerably smaller than the typical SWD variance across the image, particularly in central Texas where the SWD values are around 3°C larger than the surrounding areas. The

striping and noise simulations applied here are likely far worse than will actually occur with the ABI because a value of ±0.1°C was used, and this value is greater than the vendor-estimated worst case value of ±0.05°C. The conclusion from this analysis is that noise and striping expected from the ABI will have a negligible effect on the SWD product.

## 4. Example from Meteosat Second Generation

Since all of the information provided henceforth has been model based, it is worth showing that the detection of locally deep water vapor by the SWD works with observed satellite data. The Meteosat Second Generation series carries the Spinning Enhanced Visible and Infrared Imager (SEVIRI; Schmetz et al. 2002), an instrument with improved spatial and spectral resolution compared to the current series of GOES instruments. Its bands include a 10.8-$\mu$m IR window and a 12.0-$\mu$m dirty window, both having a 3-km subpoint footprint, allowing for the calculation of a split-window difference. Although the two bands do not match exactly with those studied above on GOES-R, the principles should still apply and allow for the detection of locally deeper low-level water vapor.

Figure 7 provides an example from 6 July 2012. The first and second columns in Fig. 7 show hourly observations of the high-resolution visible (HRV; 1-km resolution) band 12 and the 10.8–12.0-$\mu$m split-window difference, respectively, at 1000, 1100, 1200, and 1300 UTC. The area of interest is eastern Poland, which is denoted by a black polygon in all frames of Fig. 7. Column 3 is the MSG total precipitable water retrieval (Koenig and de Coning 2009); it uses the European Centre for Medium-Range Weather Forecasts (ECMWF) model 6-h forecast moisture profiles as a first guess and then adjusts the profiles based on SEVIRI-observed radiances in order to retrieve the TPW. At 1000 UTC, some high clouds can be seen in the HRV image in the northwestern portion of the black polygon, but otherwise the area is free of clouds. Clouds obscure the scene, preventing the TPW retrieval from being possible, so cloudy areas are white in column 3. At the same time, the SWD (middle column) shows a northwest–southeast-oriented maximum in the area of clear skies, but the TPW indicates fairly constant values, except immediately adjacent to the clouds. By 1100 UTC, the SWD has increased slightly but most of the region remains free of convective clouds. At 1200 UTC, a line of convective clouds can be seen in the HRV within the region of the SWD maximum, and convective initiation has occurred by 1300 UTC. The TPW shows a sudden significant increase within the region of interest at 1200 UTC, resulting in a northwest–southeast-oriented maximum that qualitatively matches the maximum in the SWD first seen before 1000 UTC. We hypothesize that the sudden increase at 1200 UTC corresponds with a new first-guess moisture field from the ECMWF. Koenig and de Coning (2009) acknowledge that "the retrieved profiles tend to retain features of the first guess," so our hypothesis is a reasonable possibility. If true, this suggests that the retrieval in this case is more sensitive to the model first guess than to the SWD observations. A retrieval less dependent on the first-guess field likely would have begun showing a local TPW maximum at or before 1000 UTC, corresponding with its first appearance in the SWD field. However, this is only a single example, and other cases may show the TPW retrieval performing differently.

This example from MSG SEVIRI has shown a local maximum in the SWD field appearing within a cloud-free area about 2 h before convective clouds began to form. Forecasters might key in on this region, and with other environmental information such as surface winds, instability, and cap strength, they might anticipate a region for convective cloud and eventually storm formation. A perfect TPW retrieval would use this SWD information (along with radiances from other bands) to indicate a local maximum in TPW likely associated with deeper low-level water vapor. But given the limitations with retrieval methods, they are imperfect, so looking also at the "raw" BT(10.8 $\mu$m)–BT(12.0 $\mu$m) field might provide forecasters with additional some lead time to convective cloud formation.

## 5. Summary and conclusions

The split-window difference has long been recognized as a tool for detecting low-level water vapor, but until the recent advent of improved satellite instruments, its utility had been limited. Most efforts have involved developing satellite-based water vapor retrievals that make use of satellite radiances and other information such as a model's first guess. This method sometimes leads to retrieval errors that result directly from model first-guess errors. Newer satellite imagers, including MSG's SEVIRI and the Advanced Baseline Imager aboard GOES-R (to be launched in 2016), have the spatial resolution sufficient to detect small-scale (2–3 km) gradients. Until water vapor retrievals are developed that make maximum use of the satellite data at full resolution, viewing the "raw" SWD field can provide forecasters with information on where low-level water vapor is locally deeper.

Radiative transfer model simulations using output from high-resolution (4 km) cloud-resolving models provide an excellent means of preparing for the real data

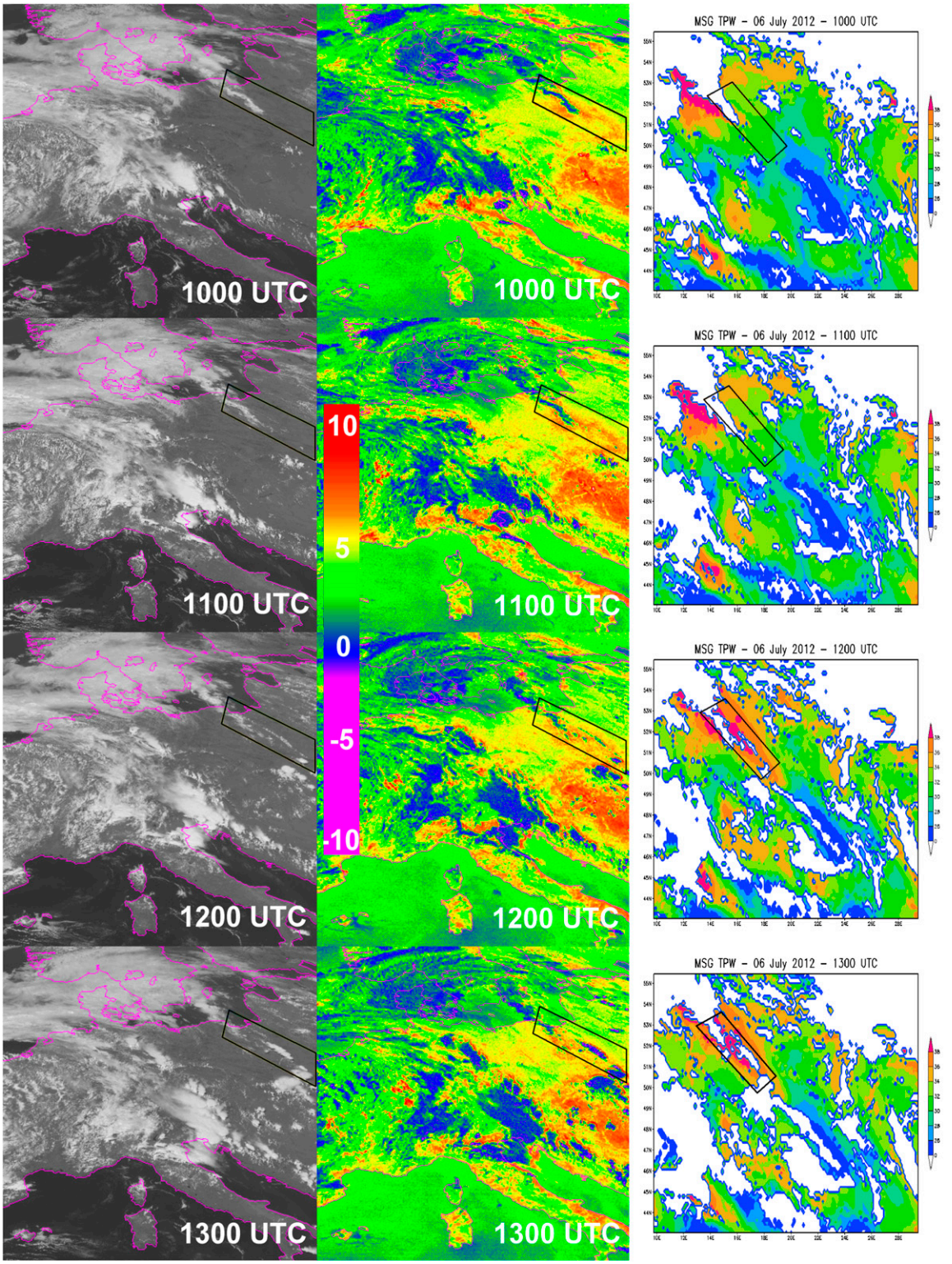


FIG. 7. (left) MSG SEVIRI band 12 (HRV), (center) MSG SEVIRI band 9–10 (10.8–12.0-$\mu$m SWD), and (right) MSG TPW retrieval, at 1000, 1100, 1200, and 1300 UTC 6 Jul 2012. The area of interest discussed in the text in eastern Poland is denoted by a black polygon in all nine frames.

that GOES-R will provide after launch. These simulations have shown that given clear-sky conditions and a temperature profile that decreases with height in the low levels (both relatively common in the central U.S. plains in the summer), low-level water vapor that is locally deeper can be inferred from the BT(10.35 $\mu$m) – BT(12.3 $\mu$m) split-window difference from the GOES-R ABI. Although the example provided from 20 May 2013 was associated with a strongly forced, synoptic-scale dryline, other examples have been collected in which mesoscale features provided a similar signal of deeper water vapor. These features include thunderstorm outflow boundaries and sea breezes.

The satellite-observed SWD depends on the vertical profile of water vapor, the temperature profile, and surface emissivity values. We have shown that variations in the SWD associated with surface emissivity heterogeneity are relatively small. The primary effect of the temperature dependence is a large-scale increase in SWD as daytime heating commences, followed by a large-scale decrease as temperatures begin to cool. But within this domain-wide diurnal trend are local maxima in the SWD that may increase faster than in the surrounding areas. These maxima are usually associated with locally deeper water vapor, sometimes resulting from horizontal surface wind convergence. Forecasters can key in on these local maxima as regions where convective clouds, and possibly storms, may eventually form.

In the future, satellite-based retrievals of temperature and water vapor need to be improved. Until these retrievals can accurately depict physical features that are evident in the raw satellite radiances, forecasters will still need to view simple imagery and band differences such as the SWD, in addition to the derived products. After GOES-R is launched in 2016, improved observations will be available to aid forecasters in the analysis of low-level water vapor.

*Acknowledgments.* This material is based on work supported by the National Oceanic and Atmospheric Administration under Grant NA090AR4320074, as well as the GOES-R Risk Reduction program. The authors thank Mat Gunshor from CIMSS for help with Fig. 1, Mark DeMaria for providing a very useful review, and helpful comments from three anonymous reviewers. The views, opinions, and findings in this report are those of the authors, and should not be construed as an official NOAA and or U.S. government position, policy, or decision.

## REFERENCES

Bikos, D., and Coauthors, 2012: Synthetic satellite imagery for real-time high-resolution model evaluation. *Wea. Forecasting,* **27,** 784–795, doi:10.1175/WAF-D-11-00130.1.

Chesters, D., L. W. Uccellini, and W. D. Robinson, 1983: Low-level water vapor fields from the VISSR Atmospheric Sounder (VAS) "split window" channels. *J. Climate Appl. Meteor.,* **22,** 725–743, doi:10.1175/1520-0450(1983)022<0725:LLWVFF>2.0.CO;2.

Dostalek, J. F., and T. J. Schmit, 2001: Total precipitable water measurements from GOES sounder derived product imagery. *Wea. Forecasting,* **16,** 573–587, doi:10.1175/1520-0434(2001)016<0573:TPWMFG>2.0.CO;2.

Griffith, P. C., A. Bell, J. Van Naarden, E. Hoffman, and C. Ellsworth, 2011: ABI flight performance predictions based on prototype model (PTM) test results. *Seventh GOES Users' Conf.,* Birmingham, AL, NOAA/NASA, P4.1. [Available online at http://www.goes-r.gov/downloads/GUC-7/poster-sessions/4-01-ABI_flight_perf_pred.pdf.]

Han, Y., P. van Delst, Q. Liu, F. Weng, B. Yan, R. Treadon, and J. Derber, 2006: JCSDA Community Radiative Transfer Model (CRTM)—version 1. NOAA Tech. Rep. NESDIS 122, 40 pp.

Jin, X., J. Li, T. J. Schmit, J. Li, M. D. Goldberg, and J. J. Gurka, 2008: Retrieving clear-sky atmospheric parameters from SEVIRI and ABI infrared radiances. *J. Geophys. Res.,* **113,** D15310, doi:10.1029/2008JD010040.

Kain, J. S., S. R. Dembek, S. J. Weiss, J. L. Case, J. J. Levit, and R. A. Sobash, 2010: Extracting unique information from high-resolution forecast models: Monitoring selected fields and phenomena every time step. *Wea. Forecasting,* **25,** 1536–1542, doi:10.1175/2010WAF2222430.1.

Kleespies, J. T., and L. M. McMillin, 1990: Retrieval of precipitable water from observations in the split window over varying surface temperatures. *J. Appl. Meteor.,* **29,** 851–862, doi:10.1175/1520-0450(1990)029<0851:ROPWFO>2.0.CO;2.

Koenig, M., and E. de Coning, 2009: The MSG global instability indices product and its use as a nowcasting tool. *Wea. Forecasting,* **24,** 272–285, doi:10.1175/2008WAF2222141.1.

Lee, Y.-K., Z. Li, J. Li, and T. J. Schmit, 2014: Evaluation of the GOES-R ABI LAP retrieval algorithm using the *GOES-13* sounder. *J. Atmos. Oceanic Technol.,* **31,** 3–19, doi:10.1175/JTECH-D-13-00028.1.

Li, Z., J. Li, W. P. Menzel, T. J. Schmit, J. P. Nelson III, J. Daniels, and S. A. Ackerman, 2008: GOES sounding improvement and applications to severe storm nowcasting. *Geophys. Res. Lett.,* **35,** L03806, doi:10.1029/2007GL032797.

Lindsey, D. T., T. J. Schmit, W. M. MacKenzie Jr., C. P. Jewett, M. M. Gunshor, and L. Grasso, 2012: 10.35 $\mu$m: Atmospheric window on the GOES-R Advanced Baseline Imager with less moisture attenuation. *J. Appl. Remote Sens.,* **6,** 063598, doi:10.1117/1.JRS.6.063598.

Ma, X. L., T. J. Schmit, and W. L. Smith, 1999: A nonlinear physical retrieval algorithm—Its application to the *GOES-8/9* sounder. *J. Appl. Meteor.,* **38,** 501–513, doi:10.1175/1520-0450(1999)038<0501:ANPRAI>2.0.CO;2.

Menzel, W. P., and J. F. W. Purdom, 1994: Introducing *GOES-I*: The first of a new generation of Geostationary Operational Environmental Satellites. *Bull. Amer. Meteor. Soc.,* **75,** 757–782, doi:10.1175/1520-0477(1994)075<0757:IGITFO>2.0.CO;2.

Moller, A. R., 2001: Severe local storms forecasting. *Severe Convective Storms, Meteor. Monogr.,* No. 50, Amer. Meteor. Soc., 433–480.

Schmetz, J., P. Pili, S. Tjemkes, D. Just, J. Kerkmann, S. Rota, and A. Ratier, 2002: An introduction to Meteosat Second Generation (MSG). *Bull. Amer. Meteor. Soc.,* **83,** 977–992, doi:10.1175/1520-0477(2002)083<0977:AITMSG>2.3.CO;2.

Schmit, T. J., M. M. Gunshor, W. P. Menzel, J. Li, S. Bachmeier, and J. J. Gurka, 2005: Introducing the next-generation

Advanced Baseline Imager (ABI) on GOES-R. *Bull. Amer. Meteor. Soc.,* **86,** 1079–1096, doi:10.1175/BAMS-86-8-1079.

——, J. Li, J. J. Gurka, M. D. Goldberg, K. J. Schrab, J. Li, and W. F. Feltz, 2008: The GOES-R Advanced Baseline Imager and the continuation of current sounder products. *J. Appl. Meteor. Climatol.,* **47,** 2696–2711, doi:10.1175/2008JAMC1858.1.

Schroedter-Homscheidt, M., A. Drews, and S. Heise, 2008: Total water vapor column retrieval from MSG-SEVIRI split window measurements exploiting the daily cycle of land surface temperatures. *Remote Sens. Environ.,* **112,** 249–258, doi:10.1016/j.rse.2007.05.006.

Seemann, S. W., E. E. Borbas, R. O. Knuteson, G. R. Stephenson, and H.-L. Huang, 2008: Development of a global infrared land surface emissivity database for application to clear sky sounding retrievals from multispectral satellite radiance measurements. *J. Appl. Meteor. Climatol.,* **47,** 108–123, doi:10.1175/2007JAMC1590.1.

Sieglaff, J. M., T. J. Schmit, W. P. Menzel, and S. A. Ackerman, 2009: Inferring convective weather characteristics with geostationary high spectral resolution IR window measurements: A look into the future. *J. Atmos. Oceanic Technol.,* **26,** 1527–1541, doi:10.1175/2009JTECHA1210.1.